

OBSERVATIONS OF NON-THERMAL AND THERMAL HARD X-RAY SPIKES IN AN M-CLASS FLARE

HAISHENG JI^{1,3}, HAIMIN WANG¹, EDWARD J. SCHMAHL², JIONG QIU⁴, and
YANAN ZHANG³

1. *Big Bear Solar Observatory, New Jersey Institute of Technology, 40386 North Shore Lane, Big Bear City, CA 92314; jihs@bbso.njit.edu*
2. *Astronomy Department, University of Maryland, College Park, MD 20742*
3. *Purple Mountain Observatory, Nanjing, 210008, P.R. China*
4. *Center for Solar Research, New Jersey Institute of Technology, NJ 07102*

ABSTRACT

We report a study of an M2.3 flare, which occurred on 2002 September 9 in the active region NOAA 0105. The observation was made at Big Bear Solar Observatory (BBSO) at the wavelength of $H_\alpha - 1.3 \text{ \AA}$, with a cadence of 40 ms. The flare was also observed by the Reuven Ramaty High Energy Solar Spectroscopic Imager (RHESSI). Three kernels appear in $H_\alpha - 1.3 \text{ \AA}$ images, two of which are conjugate kernels. The light curves of the two conjugate kernels show a correlation with that of HXR in 25 - 50 keV, however, the third one does not. We use HXR images and spectra and the time delay between the H_α blue wing emissions and HXRs to distinguish between the thermal and non-thermal character for spikes in the light curve. Among the four spikes we studied, the second spike is thermal, while the other three are non-thermal. What characterizes the thermal spike is the long time delay (~ 10 s), lack of HXR ‘footpoint’ emission and the absence of a power-law component in HXR imaging spectra. In addition, the spectrum of this spike is only well fitted by a double-temperature model with a hot (~ 25.5 MK) component and a superhot (~ 47.1 MK) component with different emission measures. The non-thermal spikes are characterized by short time delays ($\lesssim 4$ s RHESSI time resolution used in this paper), HXR ‘footpoint’ emissions and power-law spectra. The relative H_α blue wing intensities during the periods of the three non-thermal spikes are evaluated in terms of beam parameters: power-law index and X-ray flux at 10 keV. The comparison with the observations shows that the first spike of the early impulsive phase did not produce predicted H_α intensity.

Subject headings: Sun: activity — Sun: chromosphere — Sun: flares — Sun: X-rays

1. INTRODUCTION

Solar flares result from the rapid release of free magnetic energy in active regions. The dissipation of magnetic energy, which is believed to be in or above the loop top, leads to acceleration of electrons/ions to high energies and to direct heating of local plasma as well. The accelerated particle beams transport energy along magnetic field lines down to the lower atmosphere, believed to be one of the basic flare-related heating mechanisms for the chromosphere (Canfield, Gunkler, & Ricchiazzi 1984; Ding et al. 2001). The non-thermal electrons heat and ionize the chromosphere, producing optical (e.g., H_α) emissions, which are nearly simultaneous with hard X-ray (HXR) bursts.

By non-thermal ionization, the fast electrons moving down to the chromosphere can cause the electron number density to increase by an order of magnitude, and the microelectric field thus produced can cause the Stark effect (line broadening) (Svestka 1976). This effect can increase emission in the H_α line wings and thus change the line profiles (Canfield, Gunkler, & Ricchiazzi 1984; Fang, Henoux, & Gan 1993). Observations made in the wings of the H_α line can be used to study the precipitating sites of the non-thermal electrons. Also, according to the “thick-target” model, impulsive HXR emission in the early phase of a flare is generally regarded as non-thermal bremsstrahlung that accompanies the collisional degradation of non-thermal electrons in the dense chromosphere (Brown 1971; Emslie 1978). Therefore, we can expect a high correlation of some if not all H_α kernels with HXR sources both in their locations and light curves. The observed synchronism within 1 second between H_α and HXRs on some flare footpoints have been reported by a number of authors (Trottet et al. 2000; Wang et al. 2000). Based on the synchronism, they identified these footpoints as the sites of electron precipitation. Furthermore, it was believed that these sites are also HXR sources even when no spatially resolved HXR images were available.

Another mechanism for energy transport to the lower chromosphere during a flare is via a non-classical conduction front (Brown, Melrose & Spicer 1979). In this case, an obvious delay of several seconds between HXR and H_α emissions can be and has been observed (Kaempfer and Magun 1983). Thus, it may be possible for the co-existence of two kinds of heating mechanism in a same flare. Not all parts of the flare necessarily reflect the same transport process. In a similar way, for the same flare kernel, it is also unnecessary for one kind of heating mechanism to dominate and exclude the participation of another. For example, in a thermal conduction heated H_α kernel studied by Kaempfer and Magun (1983), the kernel seems to be heated by non-thermal electrons during the impulsive phase.

Whether HXR emissions are thermal or non-thermal is important for understanding the basic energy release process of a flare. There are two ways to distinguish between these mechanisms. One way to distinguish between them is by the magnitude of the time

delay between the HXR and H_α emissions. The sub-second time delay suggests non-thermal electron heating, while a longer time delay implies thermal conduction. Yet, another method is by the use of HXR spectra, which give direct information about the electron distribution. The methods can be used together with good temporal and spatial resolution; however, this has been rarely reported in the literature. In one case of high-cadence observations of an impulsive flare, Wang et al. observed a 2-3 s time delay in the very early impulsive stage. Despite this delay, they still regarded the flare as of non-thermal character because of the sub-second structures they observed. The time delay was explained as being due to the ionization timescale of the chromosphere. Their speculation could have been supported by HXR spectral data for that time period, but none existed. Until the Reuven Ramaty High Energy Solar Spectroscopic Imager (RHESSI) (Lin et al. 2002), few observations have been able to provide HXR spectral-spatial information to verify the claims of thermal and non-thermal heating mechanisms.

RHESSI is the sixth in the NASA line of Small Explorer (SMEX) and is designed to investigate particle acceleration and energy release in solar flares, through imaging and spectroscopy of hard X-ray/gamma-ray continua emitted by energetic electrons, and of gamma-rays produced by energetic ions. The spatial resolution is as fine as ~ 2.3 arc sec with a full-Sun field of view, and the spectral resolution is ~ 1 -10 keV FWHM over the energy range from the soft X-rays (3 keV) to gamma-rays (17 MeV) (Lin et al. 2002). In cooperation with RHESSI's observation, we carried out high-cadence (40 ms) observations in $H_\alpha - 1.3 \text{ \AA}$, using a CCD system with a fast frame rate installed at Big Bear Solar Observatory (BBSO) (Wang et al. 2000; Qiu et al. 2001). The high-cadence observations in the H_α blue wing, combined with excellent observing conditions at Big Bear Lake (Goode et al. 2000), provides us with both high spatial (~ 0.5 arcsec) and temporal resolutions. By observing at $H_\alpha - 1.3 \text{ \AA}$, we can locate flare kernels with less ambiguity, compared with using H_α line-center that usually shows extended bright areas called flare ribbons. Using the blue wing also lets us avoid strong thermal effects near line center and downflow effects in the red wing.

In this paper, for the first time, we try to determine whether the energy release process in a flare, especially during the time intervals of HXR spikes, is thermal or non-thermal, by exploiting the fine temporal, spatial and spectral information we can get from the high-cadence observation at $H_\alpha - 1.3 \text{ \AA}$ at BBSO and high energy spectral-spatial observations made by RHESSI.

2. OBSERVATIONS

We carried out high-cadence flare observations at the wavelength of $H_\alpha - 1.3 \text{ \AA}$ at BBSO using a Dalsa camera (256×256) with a cadence of about 40 ms. The pixel size is $0.89''$, which gives a field of view of about $228'' \times 228''$. We pointed at an active region and kept recording data for the targeted region even when there were no flares. The computer would record 20K images every time we initiated recording. The recorded non-flare data was then deleted to free disk space. If there was a flare in progress, we would let the computer record another 20K images, after it stopped recording, without deleting any recorded files in the hard disk. This allowed us to be able to record the impulsive phase of a number of flares. On 2002 September 9, we observed an M2.3 class flare in the active region NOAA 0105 (S07 E53). The recorded high-cadence data are continuous, except for a 19 s data gap, which was caused by the end and start of two recording cycles, and many small data gaps (up to several seconds), which were caused by the observation software.

One of our aims was to get a light curve for each flare kernel. Before doing this, we carried out alignments among the H_α blue wing images with a cross-correlation algorithm. The accuracy in the co-alignment was better than $1''$. Each image was then normalized to the quiet region intensity.

The RHESSI data were analyzed within the software framework developed by the RHESSI team (Schwartz et al. 2002). We obtained calibrated light curves and maps in different energy bands. In order to overlay RHESSI maps on the observed H_α blue wing images with accurate position information, we first aligned a typical H_α blue wing image with a simultaneous MDI continuum image (taken within one minute of time) to get accurate pixel resolution and pointing information. In general, the active region structure in the H_α blue wing resembles that of photosphere. This allows us to align the H_α blue wing image with a white light image with an accuracy better than $1''$.

3. RESULTS

3.1. Non-thermal and thermal

In Figure 1, the light curves in soft X-rays (SXR) (GOES 8 0.5 - 4.0 \AA in Fig. 1a), HXR (RHESSI 12 - 25 keV and 25 - 50 keV in Fig. 1b) of this flare are presented. In H_α line center, there are five ribbons, which are labeled as a1, a2, b, c and d in Figure 2. We have included the integrated light curves of these ribbons in Figure 1c-d, which we will discuss later in this paper. The flare started at 17:40 UT and lasted ~ 50 minutes in SXR and H_α

line center. The HXR emissions in the higher energy band (25 - 50 keV) lasted less than 20 minutes and started 2 minutes later than in the lower energy band (e.g. 12 - 25 keV).

As seen from Figure 1, the time profiles are different in the lower and higher energy bands of RHESSI’s observations. In the lower energy band (12 – 25 keV in Fig. 1b), the time profiles are gradual and relatively smooth. On the other hand, there are a number of impulsive spikes in the light curve of the higher energy band (25 – 50 keV in Fig. 1b). For the convenience of further reference in this paper, we choose several spikes and label them as 1 through 8. These spiky structures may indicate a number of discrete impulsive energy release processes and probably represent the non-thermal part of the HXR emissions. One of our basic goals is to find HXR associated peaks in the light curves of the H_α blue wing kernels, and thus determine the time delays with the HXR spikes.

The H_α blue wing emission of this flare lasted for about 20 minutes. As shown in Figure 2, there are, in total, four of the five H_α flaring ribbons, which lie in the field of view of the H_α blue wing images. We observed three kernels in the H_α blue wing, which correspond to ribbons a1, a2 and b in the H_α line center image.

Among the SOHO/EIT observations, there is only one 195 Å image (17:48 UT) for this flare; it shows a flaring loop. It is helpful to make a comparison regarding the locations of the HXR emissions as well as the H_α blue wing kernels with respect to this flaring loop. The overlaid images are shown in Figure 3a, in which the dotted RHESSI contours are from a Clean map in the 12 - 25 keV energy band and the solid line contours represent H_α blue wing kernels. The overlaid RHESSI map was constructed in the time period 17:47:40 - 17:48:20 UT and the H_α blue wing image was chosen for the same time (17:48 UT) as the EIT 195 Å image. It can be seen that the HXR emissions are located at the top of this flaring loop, and the two H_α blue wing kernels a1 and a2 seem to be near the footpoints of the loop seen at 195 Å. We then overlaid the EIT 195 Å image on a magnetogram taken at 17:30 UT. The magnetogram was taken at BBSO with a new digital vector magnetograph (DVMG) system (Spirock et al. 2000). We found that the brightening loop connects the two regions of opposite magnetic polarities (Figure 3b), consistent with the interpretation that it is a magnetic loop. The loop-connected H_α blue wing kernels are, therefore, conjugate kernels. From the integrated light curves of the five H_α line-center ribbons in Figure 1c-d, we can see that the light curves of ribbon a1 and a2 are quite similar but are different from those of the other three ribbons b, c, and d.

As we will see, apart from the predominant HXR emissions near the top of the loop, there are also short-lived (< 1 minute) emissions near the footpoints of the loop in higher energy bands. In the rest of this paper, we will use ‘looptop’ source to refer to the HXR emissions near the top of the loop and ‘footpoint’ sources to refer to HXR emissions near

the footpoints of the loop.

The light curves of the two conjugate kernels in the H_α blue wing are very similar. They show close correlations with the spiky light curve of HXR in the energy band of 25 - 50 keV (Figure 4). From both light curves of the two conjugate kernels, we can find corresponding peaks with respect to HXR spikes 1-8, except spike 4 and 5 due to a data gap. The H_α blue wing peaks last 10 - 20 seconds. The light curve of the third kernel b does not resemble the HXR time profile nearly as well. However, it shows some correlation with the two conjugate kernels, e.g., peak 6. That might be due to a different heating mechanism, which we will discuss later in this section. A subsequent paper will give a detailed study to the behavior of kernel b.

The time resolution of RHESSI's light curve in this paper is 4 seconds. This resolution is sufficient for our purposes. There is no sub-second first-order structure in the H_α blue wing light curve, but there are numerous second-order fluctuations, which might be real. The H_α blue wing light curves presented here are averaged ones, since we only want to get the start and peak time of the long duration peaks. Comparing them with RHESSI HXR light curve with higher time resolution will be left for subsequent efforts.

Careful examination shows that the behaviors of the two conjugate kernels a1 and a2 differ, though their light curves seem very similar. At first sight, there is a significant difference of at least 40 seconds in the timing of the initial brightening of the two kernels. Similar asymmetric behavior has also been reported and studied by Qiu et al. (2001). In the C9.0 flare they studied, the kernel k2, which brightened earlier by about 10 seconds, was more compact than the other conjugate kernel k1. In this case, we can also see that kernel a2 is a more compact source than kernel a1. It seems that a compact source might have earlier H_α brightening due to more concentrated energy deposition.

As one of the important factors in determining the heating mechanism, we have made image X-ray spectra of the 'looptop' source for a number of time periods (indicated as periods I-IV in Fig. 4). We constructed RHESSI Clean maps in the energy bands 10 - 12, 12 - 14, 14 - 17, 17 - 20, 20 - 28, and 28 - 45 keV during those periods, and obtained the integrated flux in a box around the source. The size of the box was chosen to encompass the contour of one-tenth of the peak flux. We exclude the energy bands below 10 keV in order to avoid most of the thermal part, which shows no correlation with the spiky H_α blue wing light curves. Each map is 64×64 arc sec in size (see also Sui et al. 2002). We use collimators 3, 4, 5, 6, 7, and 8 for constructing RHESSI images. The shutters were out throughout this flare.

The spectral fits are constructed by using a procedure, in which the free parameters are

varied until a minimum χ^2 fit to the count rates is obtained (Lampton, Margon & Bowyer 1976). We estimate the systematic uncertainty in the fluxes in each energy bin to be 5% of the mean count, though some authors have adjusted this to give more reasonable values of chi-squared (Holman et al. 2003). To estimate the uncertainty in constructing spectra, we made the following tests:

- Make maps with xyoffset (map center) shifted by half a pixel;
- Move the time intervals by ± 10 s;
- Shift the energy bands by ± 1 keV;
- Substitute the image algorithm Pixon for Clean.

The character of the spectral fitting (thermal or non-thermal) is not altered by these changes, and the spectral index changes are within $\pm 5\%$.

The image spectrum for the ‘looptop’ source for the time period I is shown in Figure 5a. We find a thermal distribution (Matzler et al. 1978) for this period ($\chi^2 \sim 0.76$). The thermal fit gives a superhot (~ 45 MK) source, with an emission measure of $4.26 \times 10^{46} \text{ cm}^{-3}$. This means that during the initial impulsive phase, a bulk of superhot electrons was produced instead of non-thermal electrons, thus heating the lower chromosphere by heat conduction. The thermal nature of this source is further supported by the lack of ‘footpoint’ HXR emissions from both conjugate H_α blue wing kernels during that time period. The thermal energy can then be estimated, using

$$E_{thermal} = 3k_B T \sqrt{EM \cdot V}.$$

To determine the source volume V , we take the source as being spherical in shape and take the 50% contour of its Clean image to determine the radius (Saint-Hilaire & Benz 2002). The radius of the source measures 1.4×10^9 cm, giving a total energy of $\sim 4.1 \times 10^{29}$ ergs.

For the time period II, things are different. The minimum χ^2 fitting gives a single power-law distribution ($\chi^2 \sim 1.18$). In addition, there are ‘footpoint’ HXR emissions, which are found to be cospatial with both conjugate H_α blue wing kernels (Fig. 6b). The ‘footpoint’ HXR emissions can only be seen in the higher energy band (25 - 50 keV). For comparison, we have also made a map in the lower energy band (12 - 25 keV) and overlaid it on the H_α image (Fig. 6a). The ‘looptop’ source seems to be partially cospatial with kernel a1, but we believe that this is due to a projection effect. The spectral feature and the presence of ‘footpoint’ emissions indicate a heating mechanism by non-thermal electrons. Furthermore,

the detailed light curves during this period (Fig. 6c-e) show that the start times of two H_α peaks (indicated by a dotted line) are the same within one second. Due to a data gap, we can not tell whether the maximum times of the two H_α peaks are simultaneous.

After the impulsive HXR peak time, the spectrum remains a power-law distribution (Fig. 5c). The power-law index becomes smaller. It is worth noting that the less prominent HXR spikes 2 and 3 produced more prominent peaks in the light curve of a2. By combining the time period I - III, it can be seen that unlike the usual ‘soft-hard-soft’ picture for the impulsive phase of some flares (Dennis, 1988), we have ‘thermal - non-thermal hard - non-thermal soft’ for the impulsive phase of this flare.

The spectrum for the HXR spike 6 (time period IV) can not be fitted by a single power law. Nevertheless, it can still be fitted by a double power-law distribution (Lin & Schwartz, 1987). However, if we look at the detailed light curves during this period (Fig. 7c-e), we find that there is a time delay of ~ 10 seconds between the start time of HXR spike and the relevant H_α blue wing peaks of kernel a1 and a2. The time delay, which is indicated by a dotted line and a dashed line, was confirmed by the best numerical correlation we got for the two light curve when we shifted the H_α light curve forward by 10 s. The time delay is also obvious in Figure 4 and is well beyond the time resolution of HXR light curve, and thus is believable. The time delay gives the speed of energy transport to be ~ 1500 km s $^{-1}$, if we take the distance as being 20 arc sec (Fig. 3a). The speed strongly suggests a heating mechanism by thermal conduction. In addition, there are no separate detectable ‘footpoint’ HXR emissions from the kernels a1 and a2 at this time (Fig. 7).

We try to use a thermal model to fit the spectrum for this period. However, a single temperature fit (the dotted line in Fig. 5d) is not good. The minimum χ^2 we can get is ~ 9.87 . Because of this, we try to use a double temperature thermal model to fit the spectral points, and found a good fit ($\chi^2 \sim 0.67$). The double temperature fit implies that the flaring region consists of hot plasmas (~ 25.5 MK) as well as superhot plasmas (~ 47.1 MK) with different emission measures. The emission measure of the superhot plasma is approximately one order of magnitude smaller than that of the hot plasma. From this fit, we infer that spike 6 is a thermal source with a double-temperature (multi-temperature) energy distribution. We can estimate the total thermal energy for this spike by using

$$E_{thermal} = 3k_B T_1 \sqrt{EM_1 \cdot V_1} + 3k_B T_2 \sqrt{EM_2 \cdot V_2},$$

where the subscripts refer to the hot and superhot components respectively. By assuming the volume of the superhot source to be one tenth of the volume of the whole source and using the same method to determine the source volume as above, the total energy is estimated to be $\sim 1.6 \times 10^{30}$ ergs.

There are weak ‘footpoint’ HXR emissions from kernel a1 during the time periods of spikes 7 and 8 (time periods V and VI), and the light curve of kernel a1 shows a very close correlation with HXR time profiles of that period (Fig. 8c-e). Furthermore, the time delay between HXR and H_α , which was inferred from the best numerical correlation analysis by shifting the H_α light curve backward and forward several seconds, is within the HXR time resolution (see the dotted line in Fig. 8c-e). Spectra for the periods can be fitted by power-law distributions (Fig. 5e and 5f). All these jointly indicate a non-thermal heating during the two periods.

The kernel b shows poorer temporal correlations with HXR emissions. Its initial brightening lagged that of a2 by nearly 90 seconds. In addition, the kernel can be seen moving away from the initial brightening site with a speed of about 160 km s^{-1} , which is much faster than the separation speed ($\sim 30 \text{ km s}^{-1}$) of the two conjugate kernels. There is no detectable X-ray source associated with this kernel, though there is some associated EUV brightening (see Figure 4(a)). The brightening of this kernel ended much earlier than kernels a1 and a2. Besides, in H_α line center there are two more ribbons c and d. The time profiles of H_α line center ribbons b, c, and d are different from the ones of a1 and a2 (Fig. 1c-d). The ribbons c and d are located in the same magnetic polarity region (positive), so we must classify them as one ribbon. The summed light curve of c and d looks very similar to the light curve of b. Thus, ribbons c and d may be conjugate with ribbon b, which is located in a negative magnetic polarity region.

As found by Wang et al. (2002) for other flares, the H_α line center ribbons b, c, and d may be “remote brightenings”. Also, the conjugation between ribbons c, d and ribbon b supports Wang et al.’s claim that the remote brightenings are caused by the interaction of flaring loops, which were rising, with the pre-existing higher magnetic loops, which connect the region around c and d with the region of b. Another possibility in this case is that the onset of the flare triggered magnetic instabilities of the pre-existing higher magnetic loops, which caused the remote brightening. But we still can not explain why there are no HXR emissions from the kernel b. Maybe there were no accelerated electrons to this site, thus the heating was caused by thermal conduction, or the electron density was too low for the production of HXR (Kundu, Garimov, & Schmahl, 2003).

The absence of HXR may also be due to the relatively low dynamic range of our HXR maps. At the present time, RHESSI software limits maps of flares like this to a dynamic range (defined as the ratio of the surface brightness of the brightest source to the weakest credible source), of $\sim 10 : 1$. A much higher dynamic range can, in principle, be achieved, the design goal being $\sim 100 : 1$ (Hurford et al. 2002). Thus, in Clean maps, fainter sources may exist if their surface brightness is as small as (or smaller than) about 10% of

the peak value in the map. Other factors than calibration affect the dynamic range, among them, time-variability of the sources, background (particularly at energies > 50 keV), data gaps, and photon statistics (Poisson fluctuations). In the present case, with a 20-s cadence, some of the peaks in the time profile are time-resolved, and some are not. Imaging with shorter time intervals (say ~ 10 s) might conceivably improve the time resolution, but it would increase the Poisson fluctuations. An analysis of the tradeoffs leading to an optimum mapping cadence is beyond the scope of this paper.

3.2. The observed and predicted Non-thermal heating

Canfield and Gayley (1987) gave an analytic formula for estimating the excess flare emission in the H_α blue wing. According to the formula, the dependence of the residual specific intensity, $\Delta I = I - I_0$, where I_0 is the preflare intensity in the blue wing, on the electron beam parameters is given by

$$\frac{\Delta I}{I_c} \propto \frac{(5.7 \times 10^{27})^{4/(\delta+2)} (1 \times 10^4)^{(\delta-10)/(\delta+2)}}{\delta + 2} [N_c/H]^{2\delta/(\delta+2)} q^{4/(\delta+2)} K, \quad (1)$$

where $\Delta I/I_c$ is the blue wing flare excess emission normalized to the nearby continuum I_c , δ the electron beam spectral index, N_c the cutoff stopping depth which only depends on the beam cutoff energy, H the preflare scale height, q the characteristic heating per hydrogen nucleus in units of 10^{-9} ergs s^{-1} , and K a factor only weakly dependent upon the beam parameters, which we will take as a constant in this paper. Unfortunately, we have no continuum observations, so we assume I_c to be constant during the flare. We assume an electron beam cutoff energy of 10 keV for the three non-thermal spikes, so that the cutoff stopping depth is constant for the three spikes. We get

$$\Delta I_i : \Delta I_j = F(q_i, \delta_i) : F(q_j, \delta_j), \quad (2)$$

where the subscripts stand for spike number in this paper and

$$F(q, \delta) = \frac{1 \times 10^4}{\delta + 2} [1.056 \times 10^{63} q^4]^{\frac{1}{\delta+2}}. \quad (3)$$

Following Hudson, Canfield and Kane (1978), for a power-law fit to the photon spectrum at Earth, $\Phi_{h\nu} = A(h\nu)^{-\gamma}$ photons $cm^{-2} s^{-1} keV^{-1}$, we have $\delta = \gamma + 1$ as well as a relationship between P_{10} , the energy deposited by electrons of energy above a beam cutoff energy of 10 keV, and Φ_{10} , the X-ray spectral flux at 10 keV:

$$P_{10} \propto \frac{b(\gamma)}{(\gamma - 1)} \Phi_{10}, \quad (4)$$

where $b(\gamma) = \gamma^2(\gamma - 1)^2 B(\gamma - \frac{1}{2}, \frac{3}{2})$, with $B(x, y)$ the beta function. The characteristic heating per hydrogen nucleus q is $\sim P_{10}/S$, where S is the cross sectional area of the electron beam. We assume the area is the same for the three spikes.

The beam parameters for spikes 1, 7, and 8, the kernels' excess intensities, and the kernels' areas are listed in Table 1. The kernels' areas were estimated by counting pixels whose brightness was over 25% of the mean background level within boxes where integrated the blue wing light curves were obtained. Equation (2) gives, $\Delta I_1 : \Delta I_7 = 1.0 : 0.13$, $\Delta I_1 : \Delta I_8 = 1.0 : 0.14$. The observed ratio of blue wing excess intensities for the three spikes are $\Delta I_1 : \Delta I_7 = 1.0 : 0.59$ and $\Delta I_1 : \Delta I_8 = 1.0 : 0.60$ for kernel a1 and $\Delta I_1 : \Delta I_7 = 1.0 : 0.37$ and $\Delta I_1 : \Delta I_8 = 1.0 : 0.39$ for kernel a2. We can see that the observation agrees with the theoretical predictions in the overall trend, but there still is a quantitative discrepancy between spike 1 and the two others.

To make the discrepancy clearer, the results of the comparison are shown in Figure 9. It is worth noting that the observed blue wing intensity ratio between spikes 7 and 8 agrees better with the predicted one. As has been indicated above, the less prominent HXR spikes 2 and 3, which are also softer, produced more blue wing emissions than spike 1. So we may conclude that the observed intensity for spike 1 is much lower than the predicted value.

Table 1: Parameters of the three non-thermal spikes

Spike name (i)	1	7	8
Power law index γ	5.6	7.3	7.4
X-ray flux at 10 keV Φ_{10} ¹	4.1×10^7	2.3×10^{10}	4.6×10^{10}
Predicted $\Delta I_1/\Delta I_i$	1	1/0.13	1/0.14
Excess intensity of kernel a1 ²	0.48	0.90	0.95
Area of kernel a1 ³	2.2×10^7	7.0×10^7	7.3×10^7
Observed $\Delta I_1/\Delta I_i$ at kernel a1	1	1/0.59	1/0.60
Excess intensity of kernel a2 ²	0.62	0.83	0.93
Area of kernel a2 ³	1.6×10^7	5.8×10^7	6.1×10^7
Observed $\Delta I_1/\Delta I_i$ at kernel a2	1	1/0.37	1/0.39

¹unit: photons cm⁻² s⁻¹ keV⁻¹

²relative unit

³unit: km²

4. SUMMARY AND DISCUSSION

In coordinating RHESSI’s X-ray observations with BBSO’s H_α observations, we have conducted and analyzed high-cadence observations of an M2.3-class solar flare on 2002 September 9. The BBSO observations were made in H_α line center and $H_\alpha - 1.3 \text{ \AA}$. The initial brightenings in H_α blue wing are generally regarded as being suitable to locate non-thermal electron precipitation sites (Canfield, Gunkler, & Ricchiazzi 1984). With the aid of RHESSI data, one of our scientific goals is to study the response behaviors of the solar lower chromosphere during a flare, thus to determine the importance of non-thermal electrons in the energy release process.

We have analyzed the temporal, spatial and spectral behaviors of the flare. For the first time, in combination with temporal behaviors, we use the spectral information as well as ‘footpoint’ emissions to assess whether a HXR spike is thermal or non-thermal. Among the four spikes we analyzed, three of them appear to be non-thermal while one is thermal. Thus, even for the same flare kernel site, both thermal conduction and non-thermal electron bombardment play a role in heating the lower chromosphere at different times. In obtaining these conclusions, temporal, spatial and spectral behaviors from both HXR and H_α blue wing are found to be in good agreement with each other.

In summary, in this flare, what characterizes a non-thermal spike are a power-law HXR spectrum, presence of HXR ‘footpoint’ emissions, and the short time delay (within the RHESSI’s time resolution) between H_α and HXR. On the other hand, in a thermal conduction process, no HXR ‘footpoint’ emissions were observed with the RHESSI $\lesssim 10:1$ dynamic range limitation, the spectrum cannot be fitted by a single power-law, and, most important of all, there is a long time delay regarding the response of the lower chromosphere as seen in H_α blue wing. The long time delay implies a slow energy transportation speed (1500 km s^{-1}), which in turn suggests a heating by thermal conduction.

We found that a double-temperature model fit the HXR spectrum for the time interval with a low inferred energy transportation speed. This indicates the existence of double, or even multiple, temperature structures with different emission measures during a discrete impulsive energy release process. Multithermal structures have been inferred for another flare using the SOHO Coronal Diagnostic Spectrometer (e.g. Schmelz et al. 2001). In our case the temperatures were much higher, implying the presence of “hot” and “superhot” plasmas during an impulsive energy release process.

The initial brightening of the third kernel b took place nearly 90 s after the initial brightening of kernel a2. The brightening of this kernel ended much earlier than the two conjugate kernels a1 and a2. In addition, the light curve of the third kernel shows poorer

correlation with that of the HXR light curve obtained by RHESSI, and there are no detectable HXR emissions from the kernel during the whole process of the flare.

We conclude that the third kernel, together with other ribbons shown in H_α line center, are the results of remote brightening, which may be caused by the interaction of rising flaring loops with pre-existing high magnetic loops or instabilities of the high magnetic loops triggered by the onset of the flare. We can not explain why there are no HXR emissions from the kernel b. Previous studies showed that many H_α kernels were not accompanied by HXR emissions (e.g. Asai et al. 2002) and radio sources are sometimes seen without HXR (Kundu, Garimov, & Schmahl, 2003). The lack of HXR emissions from H_α kernels may be due to either a heating role by thermal conduction as demonstrated in this paper or electron densities too low for the production of HXR. The absence of HXR may also be due to the relatively low dynamic range of our HXR maps.

We have used analytic formulae given by Canfield and Gayley (1987) and Hudson, Canfield and Kane (1978) to evaluate the observed excess flare emission in the blue wing. We infer that the observed intensity for spike 1 is much lower than the predicted value. Here it is worth mentioning that Wang et al. (1990) observed a 2-3 seconds time delay between the H_α blue wing peak and the corresponding HXR peak in the early impulsive phase of a C5.7 flare. They attributed the delay to ionization of the cool chromosphere. In this event, spike 1 is also in the early impulsive phase of the flare. So, if electron beams lose much of their energy ionizing the cool chromosphere, it might explain the low intensity of spike 1 relative to the predicted value. This could, in principle, be tested in the HXR spectrum. Kontar, Brown, and McArthur (2002) predicted that there should be a slight bump or knee in the HXR spectrum if the region that the electrons degrade in is partially neutral. The bump or knee goes away if the region is fully ionized. However, the statistics in this flare are too poor to permit that kind of analysis. The prediction can be tested by a comparison between H_α and HXR in a bigger flare.

The authors are specially grateful to an anonymous referee, who helped to improve this paper greatly. We are also grateful to the BBSO observing staff for their support in obtaining the hi-cadence data and RHESSI team for providing RHESSI data and software. The EUV data are provided by SOHO/EIT. SOHO is a project of international cooperation between ESA and NASA. This work is supported by NSF under grants ATM-0313591 and ATM-0233931, NASA under grant NAG5-10910, and ONR under grant N00014-03-1-0093. The work of JHS is also supported by CNSF 10333030. The work of E.J.S. was supported by grant NAG-5-10180 to the University of Maryland from NASA Goddard Space Flight Center.

REFERENCES

- Asai, A., Masuda, S., Yokoyama, T., Shimojo, M., Isobe, H., Kurokawa, H., & Shibata, K. 2002, *ApJ*, 578, L91
- Brown, J. 1971, *Sol. Phys.*, 18, 489
- Brown, J. C., Melrose, D. B., & Spicer, D. S. 1979, *ApJ*, 228, 592
- Canfield, R. C., Gunkler, T. A., & Ricchiazzi, P. J. 1984, *ApJ*, 282, 296
- Dennis, B. R., 1988, *Sol. Phys.*, 118, 49
- Ding, M. D., Diu, J., Wang, H., & Goode, P. R. 2001, *ApJ*, 552, 340
- Emslie, A. J. 1978, *ApJ*, 224, 241
- Fang, C., Henoux, J. C., & Gan, W. 1993, *A&A*, 274, 917
- Goode, P. R., Wang, H., Marquette, W. H., & Denker, C. 2000, *Sol. Phys.*, 195, 421
- Holman, G. D., Sui, L., Schwartz, R. A., & Emslie, A. G. 2003, *ApJ*, 595, L97
- Hudson, H. S. 1991, *Sol. Phys.*, 133, 357
- Hudson, H. S., Canfield, R. C., & Kane, S. R. 1987, *Sol. Phys.*, 60, 137
- Hurford, G. J., Schmahl, E. J., & Schwartz, R. A., et al. 2002, *Sol. Phys.*, 210, 61
- Kontar, E. P., Brown, J. C., & McArthur, G. K. 2002, *Sol. Phys.*, 210, 419
- Kopp, R. A., & Pneuman, G. W. 1976, *Sol. Phys.*, 50, 85
- Kundu, M. R., Garimov, V. & Schmahl, E. J. 2003, in preparation.
- Lampton, M., Margon, B., & Bowyer, S. 1976, *ApJ*, 208, 177
- Lin, R. P. & Schwartz, R. A., 1987, *ApJ*, 312, 462
- Lin, R. P., Dennis, B. R., & Hurford, G. J., et al. 2002, *Sol. Phys.*, 210, 3
- Matzler, C., Bai, T., Crannell, C., Frost, K. J. 1978, *ApJ*, 223, 1058
- Qiu, J., Ding, M. D., Wang, H., Gallagher, P. T., Sato, J., Denker, C., & Goode, P. R. 2001, *ApJ*, 554, 445
- Saint-Hilaire, P., & Benz, A. O. 2002, *Sol. Phys.*, 210, 287

- Schmahl, E. J., & Hurford, G. J. 2002, *Sol. Phys.*, 210, 273
- Schmelz, J. T., Scopes, R. T., Cirtain, J. W., Winter, H. D., & Allen, J. D. 2001, *ApJ*, 556, 898
- Schwartz, R. A., Csillaghy, A., K., Hurford, G. J., McTiernan, J., & Zarro, D. 2002, *Sol. Phys.*, 210, 61
- Spirock, T. J. et al. 2000, in *ASP Conf. Ser. 236, Advanced Solar Polarimetry Theory: Observation and Instrumentation*, ed. M, Sigwarth (San Francisco: ASP), 65
- Svestka, Z. 1976, *Solar Flares* (Dordrecht: Reidel)
- Sui, L., Holman, G. D., Dennis, B. R., Krucker, S., Schwartz, R. A., and Tolbert, K. 2002, *Sol. Phys.*, 210, 245
- Trottet, G., Rolli, E., Magun, A., Barat, C., Kuznetsov, A., Sunyaev, R., & Terekhov, O. 2000, *A&A*, 356, 1067
- Wang, H., Gallagher, P., Yurchyshyn V., Yang, G., & Goode, P. R. 2002, *ApJ*, 569, 1026
- Wang, H., Qiu, J., Denker, C., Spirock, T., Chen, H., & Goode, P. R. 2000, *ApJ*, 542, 1080

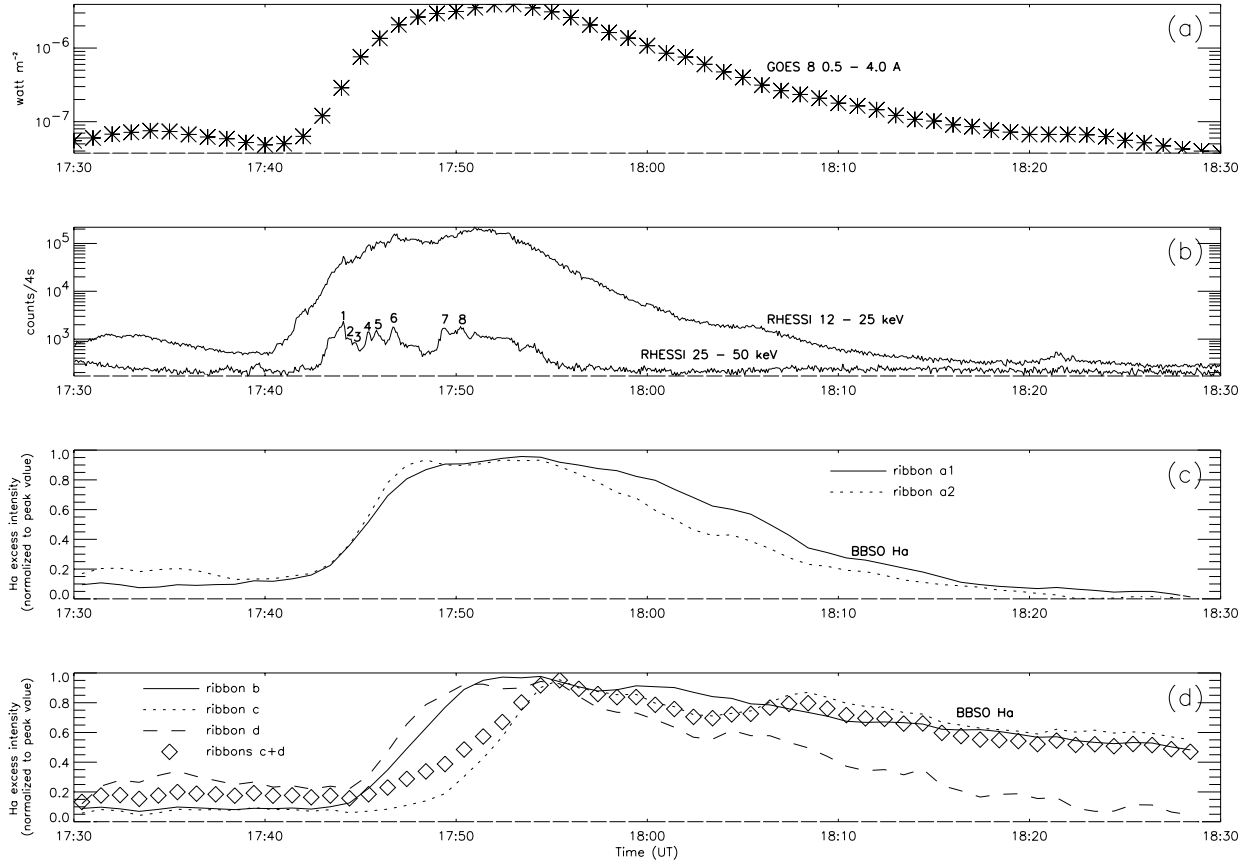


Fig. 1.— Time profiles of this flare in (a) GOES 8 0.5 - 4.0 Å (b) RHESSI hard X-ray (12 - 25 keV and 25 - 50 keV) (see Fig. 4 for an expanded plot of the spikes), and (c-d) H_α line-center excess intensity normalized to the peak value and integrated over different ribbons.

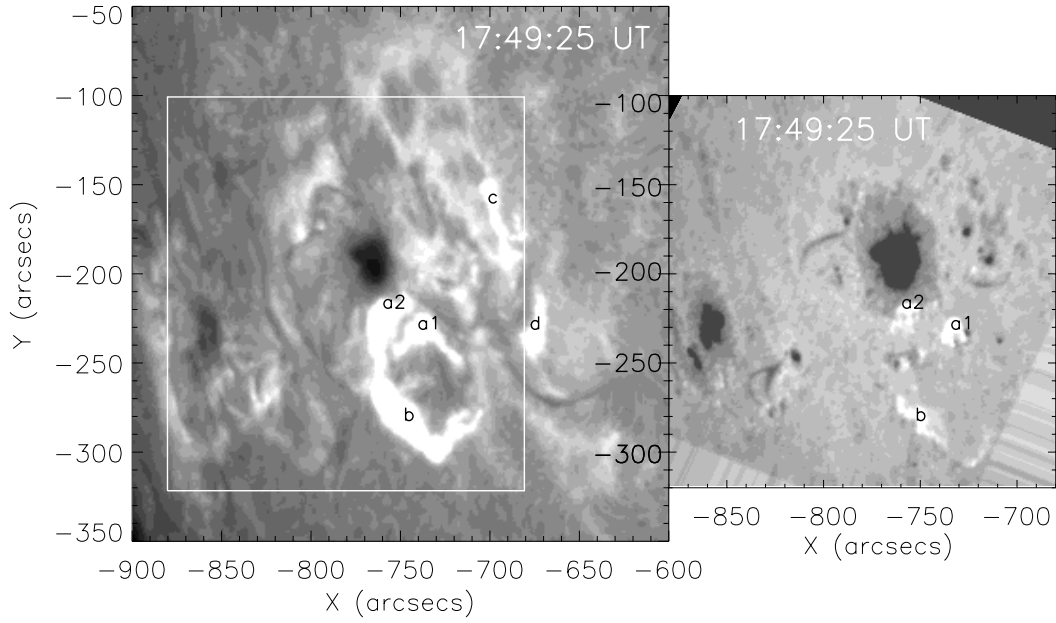


Fig. 2.— The flare observed at H_α line center (left) and $H_\alpha - 1.3 \text{ \AA}$ (right) near the flare peak time (17:49:25 UT). In H_α line center, there are five ribbons labelled a1, a2, b, c, and d. The white box in the left panel indicates the field of view of the $H_\alpha - 1.3 \text{ \AA}$ image. Among the five H_α ribbons, one (labeled as d) was out of the field of view of the $H_\alpha - 1.3 \text{ \AA}$ image. Three ribbons (a1, a2 and b) are visible in the $H_\alpha - 1.3 \text{ \AA}$ image.

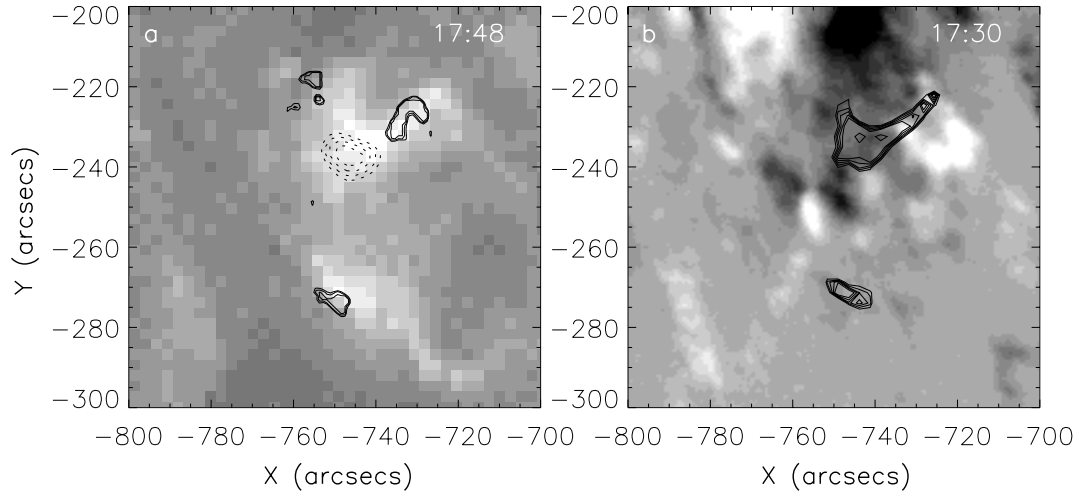


Fig. 3.— Left: the contours of the hard X-ray (12 - 25 keV) source (dotted lines) and the contours of three $H_{\alpha} - 1.3 \text{ \AA}$ kernels (a1, a2, and b from Fig. 2) are overlaid on an EIT 195 Å image taken at 17:48 UT. Right: the contours of the EIT 195 Å flaring loop from the left panel are overlaid on a BBSO magnetogram taken 18 minutes earlier.

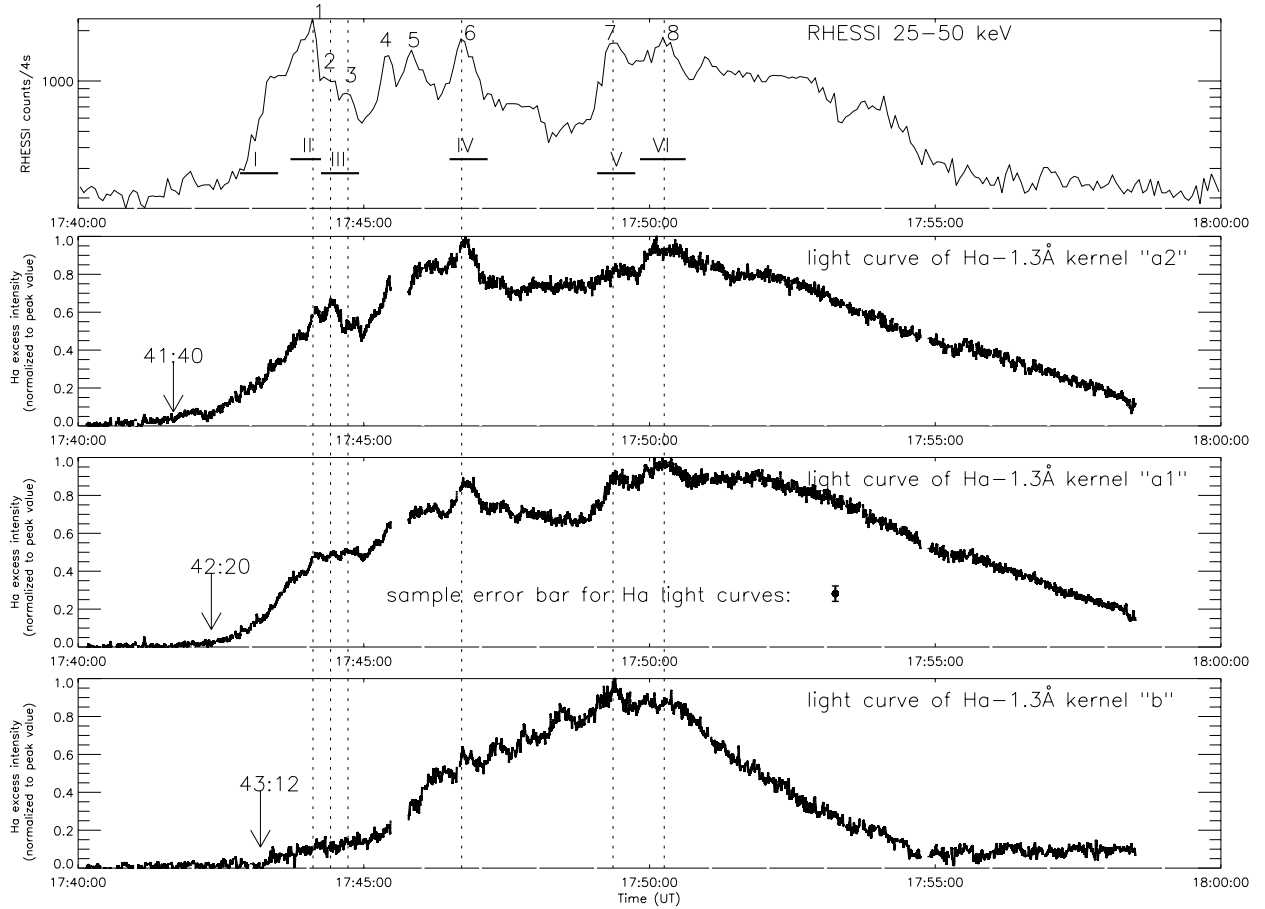


Fig. 4.— Comparison of background-subtracted and normalized time profiles of three $H_\alpha - 1.3 \text{ \AA}$ kernels with RHESSI’s HXR (25 - 50 keV) time profile, whose time resolution is 4 seconds. The data gap at 17:45:27 - 17:45:46 in the H_α light curves is due to the ending and start of two recording cycles, while the smaller gaps are caused by the observation software, which failed to record data continuously. The dotted lines indicate the peak time of the six HXR spikes. The arrows indicate the start time of the kernels’ initial brightening. The short horizontal bars with Roman numerals above them show the time period, during which we have made HXR image spectra of the ‘looptop’ source.

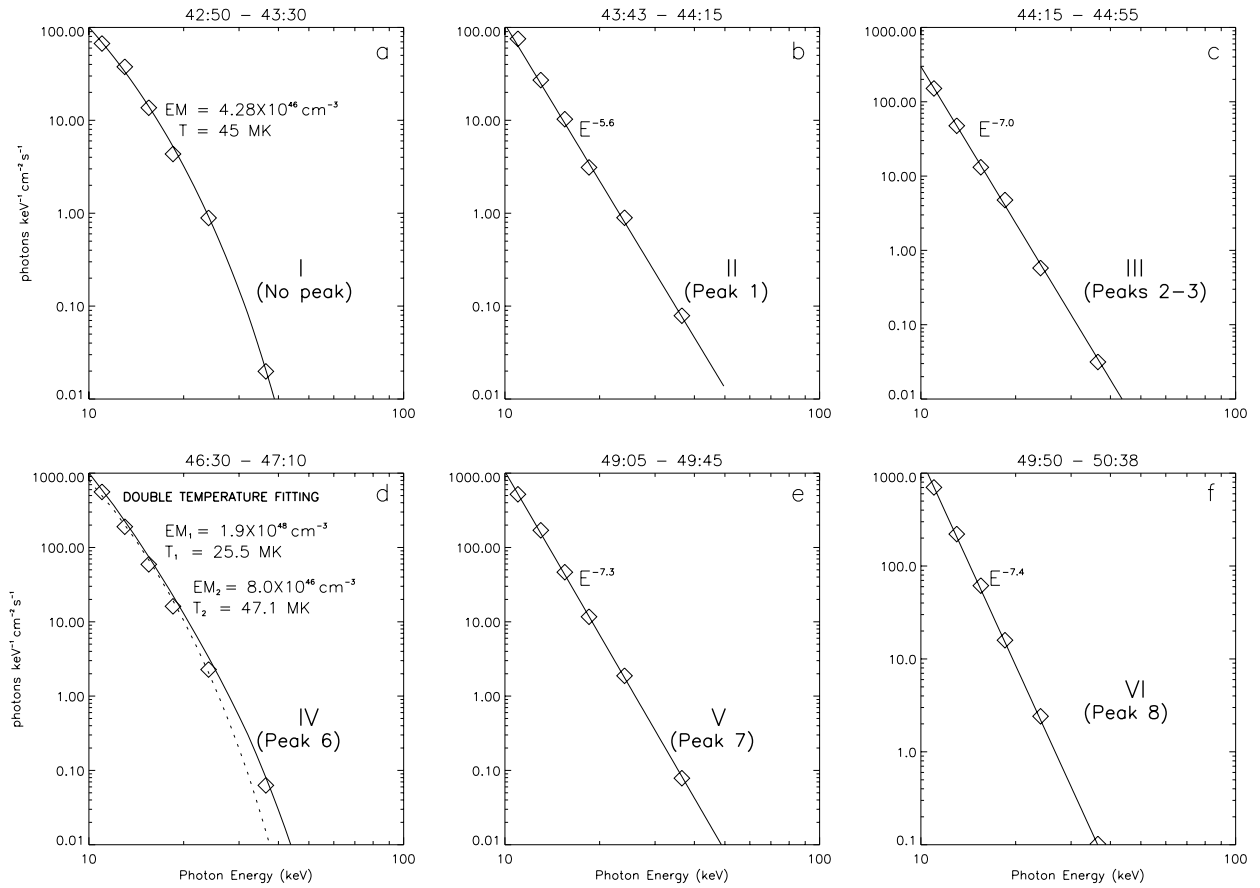


Fig. 5.— Image spectra of the ‘looptop’ source for the six time periods (I-VI) indicated in Figure 4. Each diamond represents the flux in a box around the source.

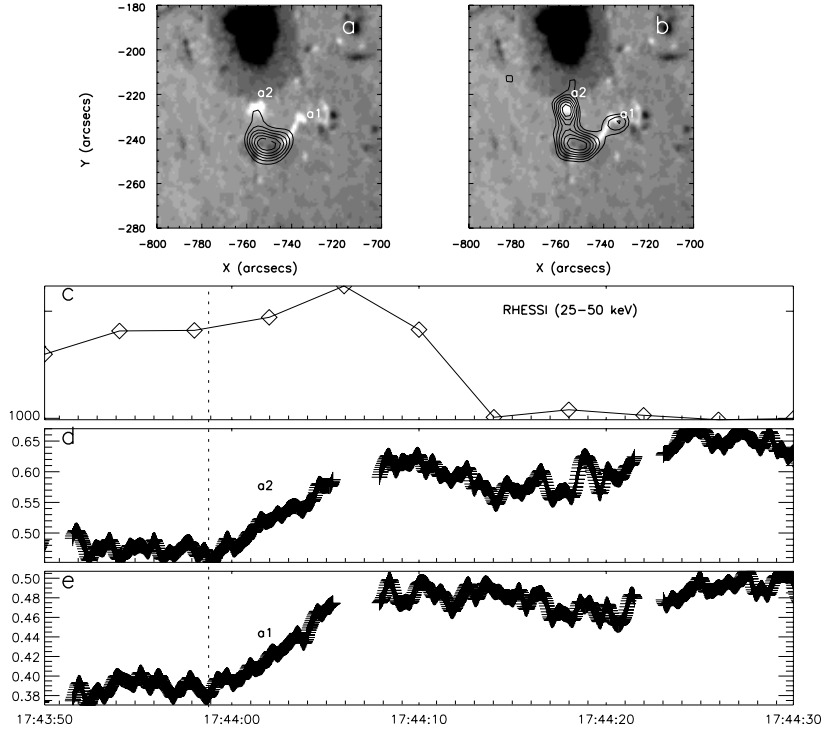


Fig. 6.— Detailed analysis of spike 1 (time period II). (a) H_α blue wing image overlaid with contours of HXR emissions in the energy band of 12 – 25 keV, showing a single ‘looptop’ source. (b) H_α blue wing image overlaid with contours of HXR emissions in the energy band of 25 – 50 keV, showing a ‘looptop’ source and two ‘footpoint’ sources, which are cospatial with the H_α blue wing kernels a1 and a2. (c-e) Enlarged light curves of HXR and H_α blue wing during this time period. The dotted line marks the start time of the two kernels.

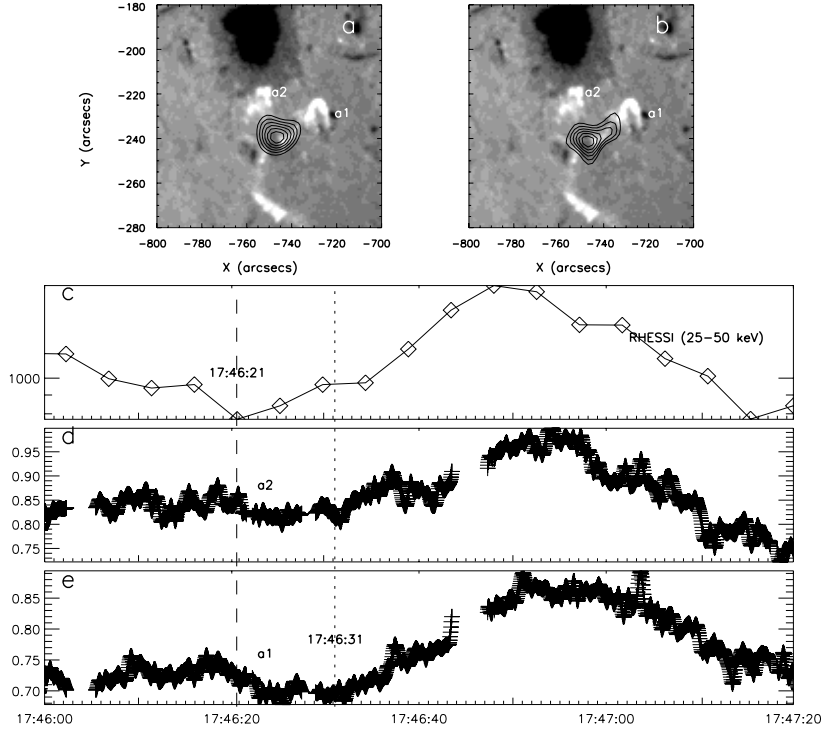


Fig. 7.— Detailed analysis of spike 6 (time period II). (a) H_α blue wing image overlaid with contours of HXR emissions in the energy band of 12 – 25 keV, showing a single ‘looptop’ source. (b) H_α blue wing image overlaid with contours of HXR emissions in the energy band of 25 – 50 keV, showing no separate ‘footpoint’ emissions. (c-e) Enlarged light curves of HXR and H_α blue wing during this time period. The dashed line marks the start time of the HXR spike, while the dotted line marks the start time of corresponding H_α blue wing spikes.

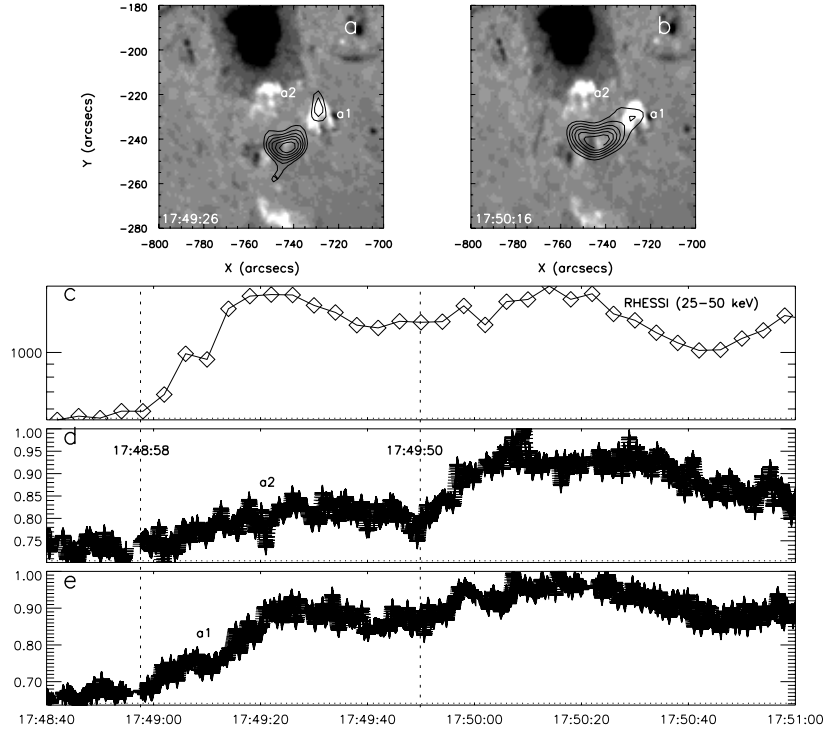


Fig. 8.— Detailed analysis of spikes 7 and 8 (time periods V and VI). (a - b) H_α blue wing images (17:49:26 & 17:50:16) overlaid with contours of HXR emissions in the energy band of 12 – 25 keV, showing ‘looptop’ sources with weak ‘footpoint’ sources from a1 during the time periods V and VI. (c-e) Enlarged light curves of HXR and H_α blue wing during this time period. The dotted lines mark the start times of the two spikes.

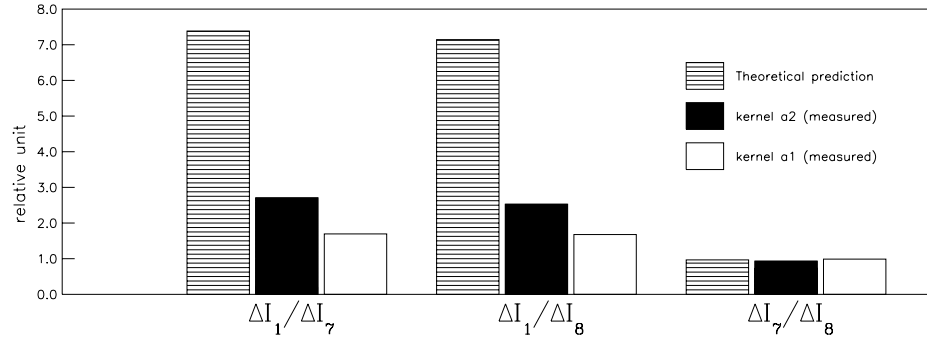


Fig. 9.— A bar graph showing a comparison between the theoretical prediction and observational results regarding non-thermal heating during the periods of the three non-thermal spikes.